Climate Dynamics (2000) 16:393–403

A. Hall · S. Manabe

Suppression of ENSO in a coupled model without water vapor feedback

Received: 26 March 1999 / Accepted: 25 October 1999

Abstract We examine 800-year time series of internally generated variability in both a coupled ocean-atmosphere model where water vapor anomalies are not allowed to interact with longwave radiation and one where they are. The ENSO-like phenomenon in the experiment without water vapor feedback is drastically suppressed both in amplitude and geographic extent relative to the experiment with water vapor feedback. Surprisingly, the reduced amplitude of ENSO-related sea surface temperature anomalies in the model without water vapor feedback cannot be attributed to greater longwave damping of sea surface temperature. (Differences between the two experiments in radiative feedback due to clouds counterbalance almost perfectly the differences in radiative feedback due to water vapor.) Rather, the interaction between water vapor anomalies and longwave radiation affects the ENSO-like phenomenon through its influence on the vertical structure of radiative heating: Because of the changes in water vapor associated with it, a given warm equatorial Pacific sea surface temperature anomaly is associated with a radiative heating profile that is much more gravitationally unstable when water vapor feedback is present. The warm sea surface temperature anomaly therefore results in more convection in the experiment with water vapor feedback. The increased convection, in turn, is related to a larger westerly wind-stress anomaly, which creates a larger decrease in upwelling of cold water, thereby enhancing the magnitude of the original warm sea surface temperature anomaly. In this manner, the interaction between water vapor anomalies and longwave radiation magnifies the air-sea interactions at the heart of the ENSO phenomenon; without this interaction, the coupling between sea surface temperature and wind stress is effectively reduced, resulting in smaller amplitude ENSO episodes with a more limited geographical extent.

A. Hall (✉)
Princeton University, Atmospheric and Oceanic Sciences Program, Princeton NJ 08544-0710, USA

Present address:
Lamont-Doherty Earth Observatory of Columbia University, Oceanography Bldg, Room 204, PO Box 1000, 61 Route 9W, Palisades, NY 10964-8000, USA
E-mail: alexhall@rosie.ldeo.columbia.edu

S. Manabe
Institute for Global Change Research/FRSGC, 7th Floor, Seavans Building-N, 1-2-1 Shibaura, Minato-ku, Tokyo 105, Japan

1 Introduction

The best-known effect of the interaction between longwave radiation and water vapor anomalies is its impact on the radiative damping of surface-tropospheric temperature anomalies. Due to the dependence of the saturation water vapor mixing ratio on temperature, as predicted by the Clausius-Clapeyron equation, anomalies of atmospheric water vapor should be correlated with surface-troposphere temperature anomalies. Since water vapor traps outgoing longwave radiation, this reduces the longwave radiative damping of the temperature anomalies. The reduction in radiative damping, in turn, increases the magnitude of the anomalies. This effect, known as water vapor feedback, has been recognized for some time (see, e.g., Manabe and Wetherald 1967). In a previous paper (Hall and Manabe 1999), we estimated the impact of water vapor feedback on internally generated surface temperature variability by comparing a coupled model simulation where water vapor anomalies are not allowed to interact with longwave radiation to a simulation where they are. There we showed that on interannual time scales and longer, there is significantly more surface temperature variability in the coupled model simulation with water vapor feedback than in the one without. This is the case at all resolved spatial scales and at all locations in the model world.

While sea surface temperature (SST) variability in the experiment without water vapor feedback is at least somewhat suppressed at all locations, the suppression is quite drastic in one region, namely the central equatorial

Pacific. This is precisely where the model exhibits a mode of variability similar to the ENSO phenomenon observed in the real climate. Thus the ENSO-like events the model simulates are much weaker when water vapor feedback is absent. Because ENSO dominates climate variability in the equatorial Pacific and plays a significant role in climate variability elsewhere, it is important to establish the cause of this ENSO suppression. This question is the subject of the present study. The most obvious answer is that equatorial Pacific SST anomalies are larger in the experiment with water vapor feedback because they are less effectively damped by outgoing longwave radiation, in the manner outlined. However, as we will show, because of differences in cloud feedback between the two models, the net radiative feedback to equatorial Pacific SST is nearly identical between the two experiments. This eliminates the possibility that differences in radiative damping of SST between the two experiments can explain the difference in ENSO-like variability. However, the interaction between longwave radiation and water vapor affects not only the radiative damping of SST at the top of the atmosphere, but also the radiative heating within the atmosphere itself. It turns out that through its influence on radiative heating, water vapor feedback increases the magnitude of ENSO events by enhancing the unstable air-sea interactions of the equatorial Pacific.

These interactions, at the heart of the ENSO phenomenon, were first identified by Bjerknes (1969). Since this mechanism is so central to our conclusions, we briefly summarize it here as background to the remainder of the work. Bjerknes (1969) observed that a warm equatorial Pacific SST anomaly leads to moist convection and low-level convergence, which in turn leads to a weakening of the climatological surface easterly winds. Since these easterly winds generate intense upwelling of cold water, a decrease in their strength implies a weakening of the upwelling as well. The decrease in the supply of cold water to the surface serves as a positive feedback to the original warm SST anomaly. This positive feedback process is crucial to the simulation and prediction of ENSO and is incorporated in some form in all models designed for the study of ENSO (Neelin et al. 1994). As we will show, the radiative heating effects of water vapor feedback are an important element in this process through their impact on the link between SST and convection.

The presentation of these results is structured as follows. First, we describe the coupled ocean-atmosphere model (Sect. 2) and the design of our experiments (Sect. 3). In Sect. 4, we present background information on the model's ENSO-like phenomenon. Then, we document in detail the suppression of ENSO in the experiment without water vapor feedback in Sect. 5. In Sect. 6, we discount the possibility that increased radiative damping in the experiment without water vapor feedback can explain ENSO suppression. We identify the actual cause of ENSO suppression in Sect. 7, in which we show how water vapor feedback affects the atmospheric stability and convection associated with an equatorial Pacific SST anomaly. Finally, in Sect. 8, we summarize our results and discuss their implications for the modeling and prediction of tropical climate.

2 Model structure and time integration

The most important features of the model used for these experiments are described in some detail in Manabe et al. (1991). It consists of a general circulation model of the world ocean coupled to an atmospheric general circulation model through exchange of heat, water, and momentum. The variables of the nine-vertical-level atmospheric component are represented in the horizontal by a series of spherical harmonics (rhomboidal truncation at zonal wave number 15) and corresponding grid point values (7.5° longitude by about 4.5° latitude gridbox size). The radiative transfer calculation includes a seasonal cycle of insolation. In addition, it takes into account the effects of clouds, water vapor, carbon dioxide, and ozone on both incoming and outgoing radiation, though only water vapor and cloud are actually predicted by the model's dynamical components. At the land surface, the model computes budgets of snow, water, and heat. The finite-difference oceanic component, with a horizontal resolution of 4.5° latitude by 3.75° longitude and 12 vertical levels, uses the Modular Ocean Model (MOM) code described in Pacanowski et al. (1991). This particular version of MOM is based, in turn, on a model described by Bryan and Lewis (1979). In addition to horizontal and vertical background sub-grid scale mixing, the model has isopycnal mixing as discussed by Redi (1982) and Tziperman and Bryan (1993). Convection occurs whenever the vertical stratification becomes unstable. Sea ice is predicted using a free drift model developed by Bryan (1969).

To prevent rapid climate drift that could distort the internally generated variability that this study seeks to diagnose, the fluxes of heat and water obtained from the atmospheric component of the coupled model are modified by given amounts before they are imposed upon the ocean surface. While these adjustments vary seasonally and geographically, they do not vary from year to year. Therefore they are unlikely to amplify or damp anomalies of sea surface salinity or temperature in a systematic way. Although the adjustments do not eliminate the shortcomings of the model (Marotzke and Stone 1995), they do prevent rapid drift of the simulated climate from realistic initial conditions.

3 Experimental design

As noted in Sect. 1, this model was integrated in two configurations to test the effects of water vapor feedback. In both cases, water vapor is variable in the hydrologic component of the model, meaning that simulated clouds and precipitation are based on humidity values predicted by the model. In the experiment without water vapor feedback (referred to hereafter as the *fixed* H_2O configuration), water vapor mixing ratios at all grid points and all nine vertical levels are fixed to their climatological mean, seasonally varying values in the longwave portion of the radiative transfer subroutine. In the experiment with water vapor feedback (referred to hereafter as the *control* configuration), on the other hand, the water vapor values predicted by the hydrologic component are passed to the longwave subroutine. The mean water vapor field used in the *fixed* H_2O experiments was calculated in the following way: first, integrating only the atmospheric component of the coupled model, and using seasonally varying, climatological sea surface temperatures and sea ice as a lower boundary condition, the daily mean values of the entire water vapor field were saved away for fifty years. Then the values corresponding to any given day of the annual cycle were averaged over all fifty years of the integration, providing a mean water vapor field for every day of the year. These mean values were supplied to the coupled model's longwave radiative transfer subroutine as the coupled integration proceeded through each day of the year.

It should be emphasized that since water vapor was fixed only in the longwave radiative transfer subroutine of the *fixed* H_2O configuration, any feedback effects due to water vapor's interaction with solar radiation are included in both configurations. The aspect of water vapor feedback relating to solar radiation is therefore not a subject of this study. For the sake of simplicity, the term 'water vapor feedback' refers only to the longwave feedback effects of water vapor throughout this article.

The model was integrated for 1000 years in each configuration, and the last 800 years of the integrations were used for analysis. Although the flux adjustment technique described in Sect. 2 minimizes climate drift, small trends remain in both experiments. For example, over the 800 years used for analysis, the *fixed* H_2O run exhibits a cooling trend of 0.009 °C per century in global-mean surface temperature. A trend of a similar magnitude exists over the same time period of the *control* run (0.035 °C per century). All such linear trends were removed from the data prior to analysis.

4 The model's ENSO-like phenomenon

As background to the diagnosis of ENSO suppression in the experiment without water vapor feedback, we present an overview of the ENSO-like phenomenon simulated by the *control* model. Others have already studied this phenomenon in very similar models. For example, Lau et al. (1992) analyzed in detail ENSO-like oscillations in a coupled ocean-atmosphere model very similar to the model used in this study, except that their model had prescribed cloudiness and no seasonal cycle. More recently, Knutson and Manabe (1994) and Knutson et al. (1997) analyzed the ENSO-like phenomena that emerge from long-term integrations of a coupled ocean-atmosphere model that includes a seasonal cycle and interactive clouds and is therefore nearly identical to the *control* model. Since much has already been done to elucidate the ENSO this type of model simulates, this overview relies to some extent on past results.

One of the classic signatures of ENSO is the pattern of correlation between sea level pressure and SST in the equatorial Pacific. During a warm El Niño event, sea level pressure is anomalously low in the eastern Pacific, and anomalously high in the Indonesian region. During a cold La Niña event, the opposite occurs: pressure is high in the east and low in the west. This pattern is well-documented in observed record (see e.g., Julian and Chervin 1978; Trenberth and Shea 1987). The top panel of Fig. 1, which shows the correlation between annual-mean SST in the central equatorial Pacific and local sea level pressure in the *control* experiment, demonstrates that this pattern is present in the model as well. Knutson and Manabe (1994) showed that model-generated, warm SST anomalies in the central equatorial Pacific are also associated with an increase in precipitation in this region. This is consistent with the sea level pressure correlation pattern shown in Fig. 1; warm central equatorial Pacific SST anomalies are correlated with negative sea level pressure anomalies, which induce convergence, moist convection, and precipitation. Since climatological mean precipitation in this model (not shown) has a maximum in the western equatorial Pacific, this constitutes an eastward migration of the tropical Pacific rain belt during a simulated El Niño event, much as observed in the real world (see Rapelewski and Halpert 1987). Lau et al. (1992) noted other features: a simulated El Niño event is associated with a collapse of the climatological surface easterlies across nearly the entire Pacific, which is dynamically consistent with the pressure drop and increase in moist convection. This, in turn, is associated with a cessation of upwelling of relatively cold water across most of the central equatorial Pacific (see Fig. 9 of Lau et al. 1992), which reinforces the warm SST anomaly. These facts demonstrate that the unstable air-sea interactions at the heart of the ENSO phenomenon, discussed in Sect. 1, are at work in this model.

These unstable air-sea interactions serve as a positive feedback that enhances the magnitude of an El Niño or La Niña event once it occurs. In addition, this model succeeds in simulating, if only qualitatively, some of the mechanisms thought to be most important to the transition from the El Niño to the La Niña phases of ENSO. For example, Knutson et al. (1997) demonstrated that the propagation of subsurface ocean temperature anomalies across the equatorial Pacific plays a central role in this model's ENSO, just as it apparently does in the real world (Chao and Philander 1993). For this reason, they classified the mechanism behind this model's oscillation from one phase of ENSO to another as akin to the more realistic 'delayed oscillator' of Schopf and Suarez (1988), rather than the less realistic 'SST mode' of Neelin (1991). For further information on the realism of model-generated ENSO phenomena, including a detailed life cycle description of a typical simulated ENSO event, see Knutson et al. (1997).

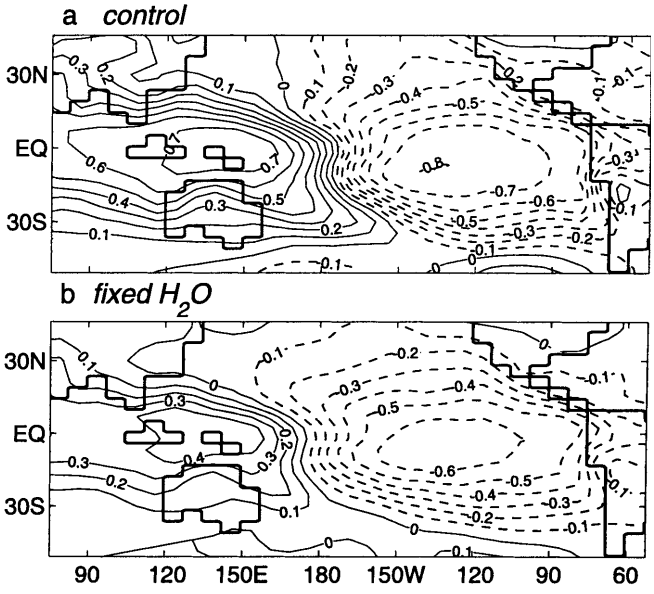

Fig. 1 **a** The geographical distribution of the correlation between local, annual-mean sea level pressure and annual-mean SST averaged over the central equatorial Pacific (4.5°S–4.5°N, 172.5°E–120°W). Data were taken from the *control* experiment. Solid lines indicate regions where the correlation is positive, while dashed lines indicate regions where the correlation is negative. **b** As in **a**, except for the *fixed* H_2O case

This qualitatively realistic ENSO-like phenomenon results in a local maximum in standard deviation of annual-mean SST in the equatorial Pacific, as seen in the top panel of Fig. 2. However, as noted in Hall and Manabe (1999), the amplitude of the SST variability in the *control* model is substantially smaller than observed throughout the central equatorial Pacific, in spite of the qualitative realism of the model's ENSO. Moreover, the model's ENSO-related SST variability is too confined to the central equatorial Pacific; in the real world, El Niño events are often characterized by substantial warming and expansion of the tropical Pacific rain belt from the central equatorial Pacific all the way to the coast of South America (Rasmusson and Carpenter 1982). One of the main reasons the model's ENSO is too small in both amplitude and geographical extent is the relatively coarse resolution of the model. For example, when the resolution of the model is increased from rhomboidal 15 truncation to rhomboidal 30, the amplitude of the ENSO-like phenomenon increases by about 60% (T. Knutson personal communication).

5 Documentation of ENSO suppression

In this section we characterize the ENSO suppression in the *fixed* H_2O experiment. It was noted in Sect. 4 that the model's ENSO-like phenomenon results in an enhance-

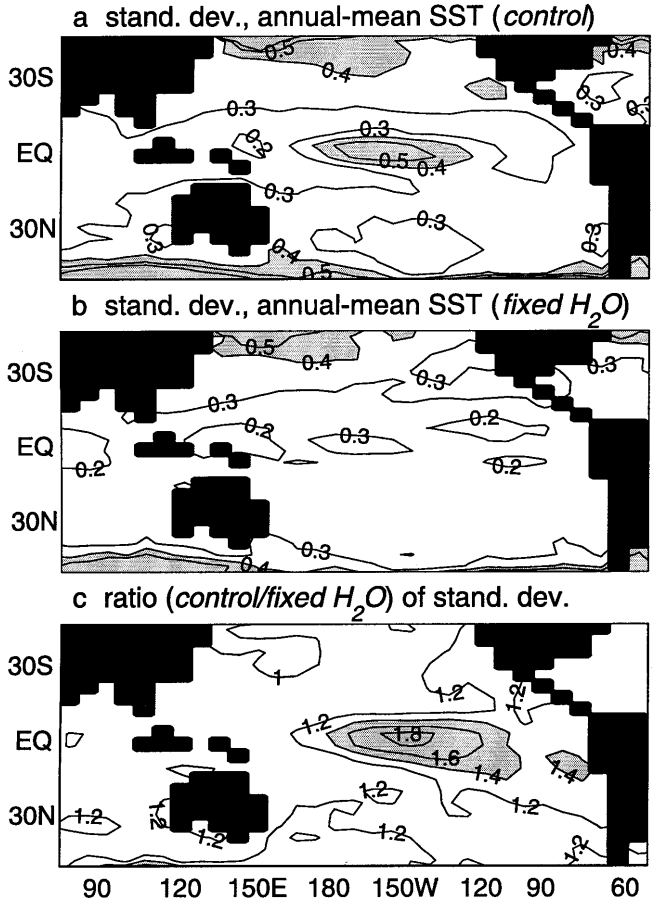

Fig. 2 **a** Geographical distribution of standard deviation of annual-mean SST (°C) from the *control* experiment. Regions where the standard deviation exceeds 0.4 °C are shaded. **b** As in **a** except for the *fixed* H_2O experiment. **c** Geographical distribution of the ratio (*control*/*fixed* H_2O) of standard deviation of annual-mean SST. Regions where the ratio exceeds 1.4 are shaded

ment of SST variability in the central equatorial Pacific (see Fig. 2a). Figure 2b shows the standard deviation of SST variability in the *fixed* H_2O experiment. The relative maximum in standard deviation in the equatorial Pacific, although present, is barely noticeable in this case. That the removal of water vapor feedback has a very striking effect on SST variability in the region most affected by the model's ENSO is made even clearer by Fig. 2c, which shows the ratio (*control*/*fixed* H_2O) of annual-mean SST standard deviation. While the ratio of standard deviation hovers between 1 and 1.2 over most the area shown, it is much greater in the central equatorial Pacific than elsewhere, reaching values around 1.8. Thus the background effect of water vapor feedback is a 10 to 20% enhancement of local SST variability, whereas in the region where SST is most affected by ENSO, water vapor feedback enhances variability by 40 to 80%.

The near absence of a relative maximum in SST variability in this region when water vapor feedback is removed might suggest that the ENSO-like phenomenon itself is absent in the *fixed* H_2O experiment. However, this is not the case. Figure 1b shows the correlation

Table 1 The regressions between annual-mean time series of top-of-the-atmosphere radiative fluxes (W/m^2) averaged over the central equatorial Pacific (4.5°S–4.5°N, 172.5°E–120°W) and SST (°C) averaged over the same region

	Control	*Fixed* H_2O
Clear-sky OLR	0.33	2.32
All-sky OLR	−4.83	−3.23
All-sky ISR	−2.48	−1.32
Net (OLR-ISR)	−2.35	−1.91

between SST in the equatorial Pacific and local sea level pressure in the experiment without water vapor feedback. While the correlations are somewhat smaller in the *fixed* H_2O case, warm SST in the central equatorial Pacific is still well-correlated with low pressure anomalies in the central and eastern Pacific and high pressure anomalies in the Indonesian region. Thus the *fixed* H_2O experiment exhibits the same classic teleconnection pattern associated with ENSO. This suggests that an ENSO-like phenomenon is present in the experiment without water vapor feedback, but that its magnitude is much smaller than in the *control* experiment.

Comparing Fig. 2a, b, another intriguing difference between two experiments is apparent: the region of maximum standard deviation of SST in the *control* experiment extends significantly further east than its *fixed* H_2O counterpart. This difference is also evident in Fig. 2: the region of anomalously high ratio of standard deviation of SST stretches even further east than the relative maximum in *control* SST standard deviation, across the central and eastern equatorial Pacific nearly to the coast of South America. This indicates that the the ENSO-like phenomenon in the experiment without water vapor feedback, in addition to being smaller in magnitude, is substantially more restricted to the central equatorial Pacific than in the *control* experiment.

6 Radiative feedbacks to SST

Here, we explore the possibility that differences in radiative feedbacks could be responsible for the reduced amplitude of the ENSO-like phenomenon in the *fixed* H_2O experiment. The increase in longwave radiative damping of SST when water vapor feedback is removed is the most obvious way to reduce the magnitude of the ENSO-associated SST anomalies. To see how important this effect could be, we compare the strength of the clear-sky longwave radiative damping of SST in this region in both experiments. The top row of Table 1 shows the regressions between annual-mean, clear-sky outgoing longwave radiation (OLR) at the top-of-the-atmosphere averaged over the central equatorial Pacific and SST averaged over the same region. The model calculates clear-sky OLR off-line by excluding clouds from the radiative transfer calculation. This calculation takes place at every radiative time step of the integration. The regression is about seven times larger in the *fixed* H_2O

case. Thus if clouds had no effect on radiation, SST would be much more effectively damped by longwave radiation in the experiment without water vapor feedback. This result confirms that an increase (decrease) in SST in the central equatorial Pacific is associated with an increase (decrease) in atmospheric water vapor and greenhouse trapping.

By itself, this result might also be taken as evidence that it is the increased radiative damping of SST resulting from the elimination of water vapor feedback that decreases the magnitude of ENSO-related SST anomalies. However, actual model SST is affected by the longwave radiation calculation that includes the effects of clouds. Accordingly, the second row of Table 1 shows the regressions between annual-mean all-sky OLR at the top-of-the-atmosphere and SST. Differences between the clear-sky and all-sky regressions can be attributed to the effects of clouds. Surprisingly, unlike the clear-sky OLR case, both regressions are strongly negative. The ENSO region is unusual in this regard. For example, at all extratropical locations, the regressions between local OLR and surface temperature (not shown) are positive in both models, and outgoing longwave radiation damps surface temperature. While it is true that in some regions of the tropical oceans outside the central equatorial Pacific, the regression between OLR and SST is slightly negative, nowhere in the world is the regression nearly as negative as in the central equatorial Pacific. Here, OLR fluctuates so as to reinforce SST anomalies.

The only way an increase (decrease) in SST could result in such a large decrease (increase) in OLR is if cloudiness increases (decreases) significantly along with the SST anomaly. The fact that the cloud feedback operates in this manner and is unusually strong in the central equatorial Pacific may be verified by examining the relationship between cloudiness anomalies and SST anomalies over the entire ocean. To quantify this relationship, we first calculated correlations between annual-mean cloud fraction and SST at every level and every grid point. Then we calculated the mass-weighted vertical average of these correlations to collapse this information to two dimensions. The top panel of Fig. 3 shows the results of this calculation for the *control* experiment. The central equatorial Pacific stands out like a bull's eye. The vertically averaged correlations, greater than 0.4 at the center of the bull's eye, are higher here than any other region of the world ocean. This confirms that a warm SST anomaly in the central equatorial Pacific is accompanied by a systematic increase in cloudiness and greenhouse trapping, resulting in a strongly negative relationship between OLR and SST.

The regression between OLR and SST is less negative in the *fixed* H_2O case, indicating that this effect, though undoubtedly present, is somewhat weaker in the experiment without water vapor feedback. It is significant, however, that the difference between the all-sky regressions is smaller than the difference between the clear-sky regressions. This suggests that the absence of water vapor feedback in the *fixed* H_2O experiment may be

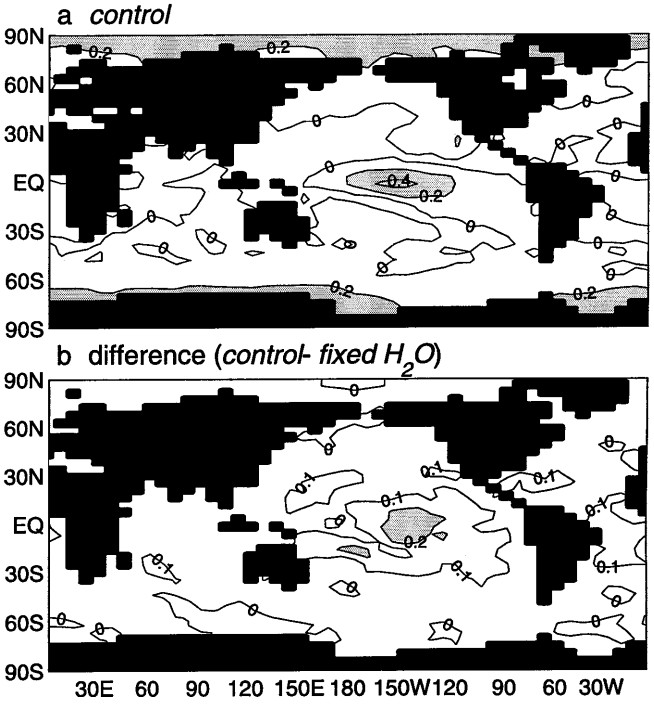

Fig. 3 **a** Geographical distribution of the mass-weighted, vertically-averaged correlation between cloud fraction and SST for the *control* experiment. Regions where the vertically-averaged correlation exceeds 0.2 are shaded. **b** Geographical distribution of the difference (*control-fixed* H_2O) in the mass-weighted, vertically-averaged correlation between cloud fraction and SST. Regions where the difference exceeds 0.2 are shaded

somewhat compensated by a more positive cloud feedback. That the cloud feedback is different in the two models is made clearer by focusing on shortwave rather than longwave radiative feedbacks. The regressions between incoming shortwave radiation (ISR) at the top of the atmosphere and SST are shown in the third row of Table 1. They are negative in both cases, implying significant damping of SST anomalies due to solar radiation. This is the result of the same cloudiness changes noted in the discussion of the regressions between OLR and SST and documented in Fig. 3a; an increase (decrease) in SST results in an increase (decrease) in cloudiness, which increases (decreases) local albedo and therefore decreases (increases) ISR. However, the regression is about twice as large in the *control* case. Thus for a given increase in SST, the ISR decrease is larger in the experiment with water vapor feedback. Taking into account only the solar component of the radiative balance, there is more negative feedback in the *control* experiment in the central equatorial Pacific. Thus cloud feedback does not have the same strength in the two models; in this region, the disabling of water vapor feedback has a large effect on cloud feedback.

It should be emphasized that this drastic change in cloud feedback as a result of the removal of water vapor feedback does not occur elsewhere. We may demonstrate this point by examining the differences between the two model configurations in the relationship between

cloudiness and SST over the entire model ocean. Figure 3b shows the geographical distribution of the difference (*control-fixed H_2O*) in the vertically averaged correlation between annual-mean cloudiness and SST. This panel demonstrates that there is no systematic difference in the relationship between cloud fraction and SST, except in a broad region centered on the equatorial Pacific. In the central equatorial Pacific, the difference in vertically averaged correlation is quite large, exceeding 0.2. Here anomalies of cloudiness are much better correlated with SST in the experiment with water vapor feedback. This is consistent with the preceding discussion of the longwave and shortwave feedbacks to SST. Thus with the striking exception of the region that is the focus of this article, cloud feedback is not substantially different in the two models.

To summarize the results of this section so far, the regressions between OLR and SST indicate that ENSO-related SST anomalies are affected by more positive feedback in the *control* experiment, whereas the regressions between ISR and SST indicate more positive feedback in the *fixed H_2O* experiment. To determine which competing effect dominates, we calculated the regressions between net radiation (OLR-ISR) and SST, shown in the fourth row of Table 1. Although the regression is slightly smaller in the *control* experiment, the relationship between net radiation and SST is actually quite similar in both cases; in the *control* experiment, the additional negative feedback due to the solar aspect of cloud feedback nearly cancels out the additional positive feedback stemming from the longwave aspect of water vapor feedback. Surprisingly then, it is very unlikely that differences in radiative feedbacks can account for the smaller magnitude of the ENSO-related SST fluctuations in the experiment without water vapor feedback. We search for the true mechanism in Sect. 7.

7 Water vapor feedback and atmospheric stability

We showed in the previous section that there is no net decrease of positive feedback to equatorial Pacific SST when water vapor feedback is removed. However, the only structural difference between the *control* and *fixed H_2O* models is that water vapor anomalies are not allowed to interact with longwave radiation in the *fixed H_2O* experiment. The suppression of ENSO in the experiment without water vapor feedback must somehow be rooted in radiative processes affected by water vapor. The only quantity that water vapor affects directly as it interacts with longwave radiation, other than outgoing longwave radiation at the top and bottom of the atmosphere, is radiative heating throughout the atmosphere itself. It therefore seems likely that water vapor feedback influences ENSO through its effect on radiative heating. In this section, we test this hypothesis.

We begin by examining the radiative heating anomalies themselves that are associated with typical SST anomalies in the equatorial Pacific. Figure 4 shows a longitude-height cross section at 2.25°N of the regression between annual-mean radiative heating throughout the atmosphere and underlying SST for both experiments. The longitudes shown range from 150°E, the approximate longitude of the east coast of Australia, to 90°W, the approximate longitude of Panama. This cross section goes directly through the heart of the maximum in SST standard deviation associated with the model's ENSO-like phenomenon (see Fig. 2). In the center of the equatorial Pacific, a typical SST anomaly in the *control* experiment is associated with a very large positive radiative heating anomaly in the lower troposphere. The anomaly is much smaller in the upper troposphere. This vertical structure reduces the gravitational stability of the atmosphere, producing conditions more favorable to convection. The opposite situation exists in the *fixed H_2O* experiment. Here the anomaly in radiative heating tends to be more uniform throughout the troposphere, with slightly more radiative heating in the upper troposphere. This vertical structure has a stabilizing influence, inhibiting convection.

Given the differing vertical structures of radiative heating associated with typical SST anomalies in the two experiments, one would expect a typical SST anomaly to be associated with more convection in the *control* than the *fixed H_2O* experiment. We illustrate this point in Fig. 5, which shows the regressions in both experiments between annual-mean pressure velocity and local SST for the same longitude-height cross section as Fig. 4. This model employs pressure as a vertical coordinate, so pressure velocity is a measure of motion in the vertical direction. Negative values of pressure velocity indicate upward motion. Upward motion, in turn, occurs when convection is present. The updraft anomaly associated

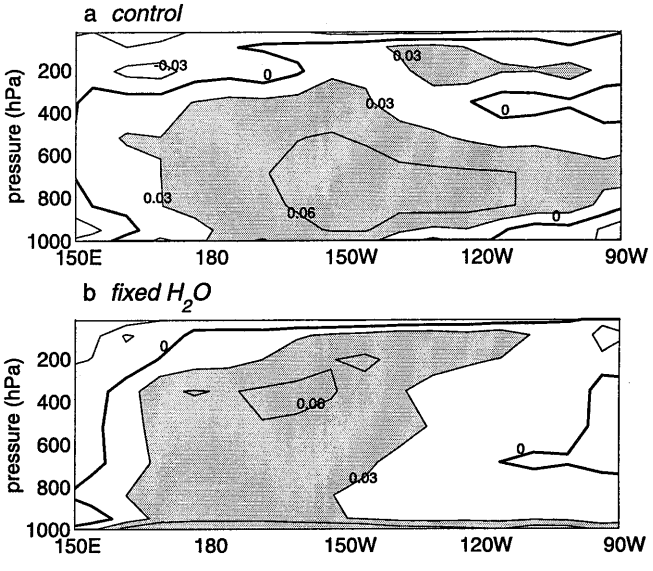

Fig. 4 **a** Longitude-height cross-section at 2.25°N of the regression between annual-mean radiative heating (°C/day) and SST (°C) in the *control* experiment. Regions where the regressions exceed 0.03 are shaded. The zero contour is thickened for clarity. **b** As in **a**, except for the *fixed H_2O* case

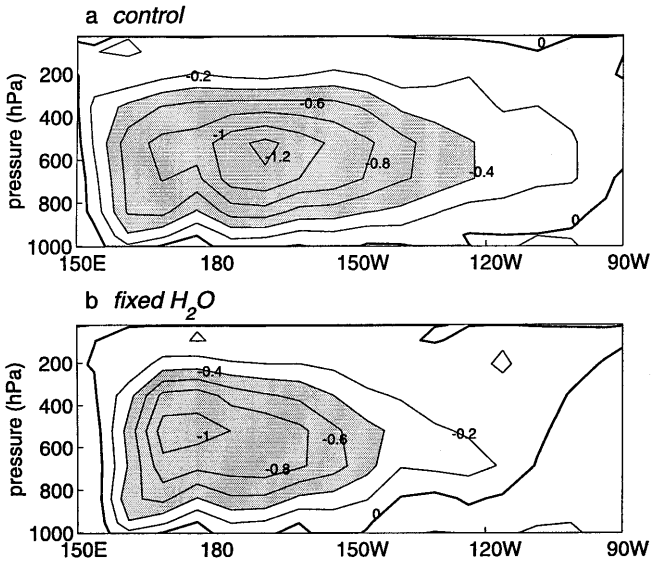

Fig. 5 **a** Longitude-height cross-section at 2.25°N of the regression between annual-mean pressure velocity (units: day^{-1}) and SST (°C) in the *control* experiment. The regressions were divided by 10^6 before plotting to simplify contour labels. Regions where the regressions are less than −0.4 are shaded. The zero contour is thickened for clarity. **b** As in **a**, except for the *fixed H_2O* case

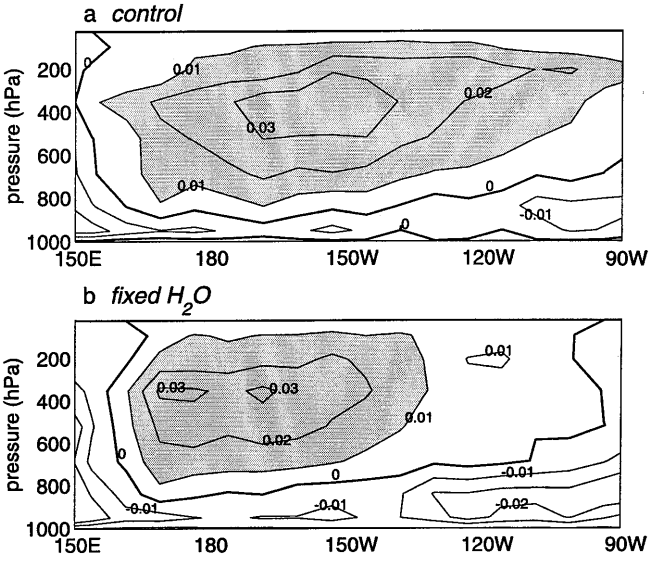

Fig. 6 **a** Longitude-height cross-section at 2.25°N of the regression between annual-mean cloud fraction and SST (°C) in the *control* experiment. Regions where the regressions exceed 0.01 are shaded. The zero contour is thickened for clarity. **b** As in **a**, except for the *fixed H_2O* case

with a given SST anomaly is much larger in the *control* case, especially in the central and eastern portions of the basin, where the ENSO suppression in the experiment without water vapor feedback is most noticeable. This indicates that more convection is associated with a given SST anomaly in the *control* case.

We have already noted in Sect. 6 that anomalies of cloudiness are better correlated with equatorial Pacific SST in the experiment with water vapor feedback. The reason for this difference is now clear: SST anomalies in the *control* experiment are associated with a more unstable vertical profile of radiative heating, which leads to more convection. Convection in turn produces cloudiness anomalies by enhancing the penetration of moisture into the atmosphere and inducing condensation. We may verify that a typical equatorial Pacific SST anomaly in the *control* experiment is related to a larger cloudiness change in the atmosphere above by examining the regressions between annual-mean cloud fraction and local SST. These are shown in Fig. 6 for the same cross section as Figs. 4 and 5. Consistent with the relationship between SST and convection, the changes in cloudiness are indeed much larger and more widespread in the upper troposphere in the *control* experiment, especially in the central and eastern portions of the basin.

So far, we have documented the fact a typical SST anomaly in the equatorial Pacific is related to much more convection and cloudiness in the *control* experiment because the vertical profile of radiative heating has a destabilizing influence on the atmosphere in the *control* experiment. We devote the remainder of this section to diagnosing the cause of the difference in vertical structure of radiative heating shown in Fig. 4. Since this

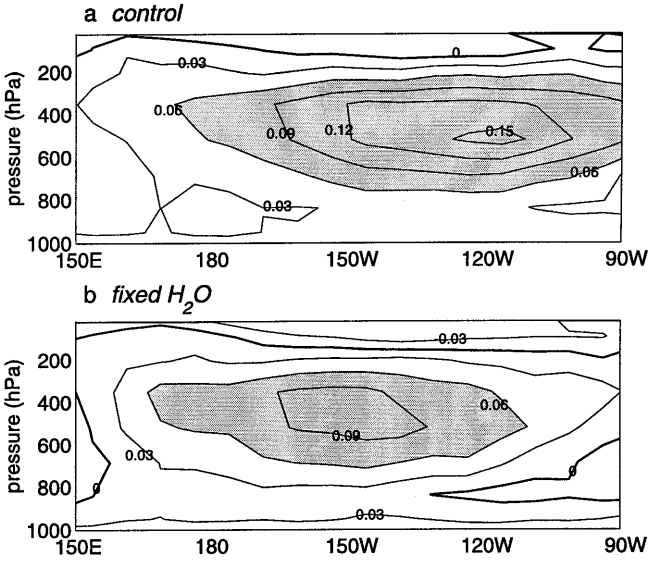

Fig. 7 **a** Longitude-height cross-section at 2.25°N of the regression between annual-mean fractional changes in water vapor and SST (°C) in the *control* experiment. Regions where the regressions exceed 0.06 are shaded. The zero contour is thickened for clarity. **b** As in **a**, except for the *fixed H_2O* case

difference must be traced ultimately to the interaction of water vapor and longwave radiation, we first show the changes in atmospheric water vapor associated with a typical equatorial Pacific SST anomaly. Figure 7 shows a longitude-height cross section of the regression between fractional changes in annual-mean water vapor and local SST for the equatorial Pacific cross section. Regressions were calculated using fractional changes in absolute humidity, rather than absolute humidity itself,

to focus directly on the radiative impact of water vapor fluctuations. Since longwave absorptivity due to water vapor is approximately proportional to the logarithm of the water vapor mixing ratio in the troposphere, fractional changes in water vapor are roughly proportional to changes in atmospheric absorptivity due to water vapor. Examining the *control* panel, it is clear that there are very large fractional increases in water vapor for a given change in SST. This is especially true around 500 hPa in the central to eastern portion of the basin. Of course, the fractional increases in water vapor shown in the identical plot for the *fixed* H_2O case do not affect the longwave radiative heating in the atmosphere. Here we merely note that in the experiment without water vapor feedback, a 1 °C SST anomaly is also associated with large fractional increases in water vapor at approximately the same vertical level as the *control* case. However, the increases are generally smaller and the maximum increases are centered further west.

Through their effect on longwave radiation, the fractional changes in water vapor shown in Fig. 7a would tend to cool the upper troposphere and heat the lower troposphere. Thus the longwave effects of water vapor may be the main reason why the vertical profile of radiative heating shown in the *control* panel of Fig. 4 is large in the lower troposphere and small in the upper troposphere, while the opposite is true of the *fixed* H_2O case. However, while water vapor feedback could account for this difference, the cloudiness changes associated with a typical equatorial Pacific SST anomaly also differ between the two experiments, as demonstrated by Fig. 6. Clouds also have a significant impact on both solar and longwave radiative heating. To determine whether cloud or water vapor anomalies are mainly responsible for the difference in the radiative heating profiles observed in Fig. 4a, b, it is necessary to separate the effects of clouds and water vapor on radiative heating. To accomplish this task, we imposed the cloud and water vapor changes shown in Figs. 6 and 7 separately on an offline version of the model's radiative transfer subroutine.

Before discussing the results of this calculation, we first verify that the off-line version of the radiation code is capable of reproducing the radiative heating cross sections shown in Fig. 4. This is an issue for two reasons. First, as the actual model integration proceeds, the model predicts either cloud or clear sky. The data output from the model, however, contains only cloud fractions, representing the fraction of time a particular grid point is cloudy. Thus the actual radiative transfer subroutine processes either clear or cloudy sky at each grid point and model level, while the off-line version must process fractional cloudiness values. This difference could lead to an error in the off-line calculation. Second, even if the actual radiative transfer code and its offline version both processed fractional cloudiness values, the radiative heating rates based on time mean cloudiness could still differ from the time mean radiative heating rates based on instantaneous cloudiness. To verify that these errors

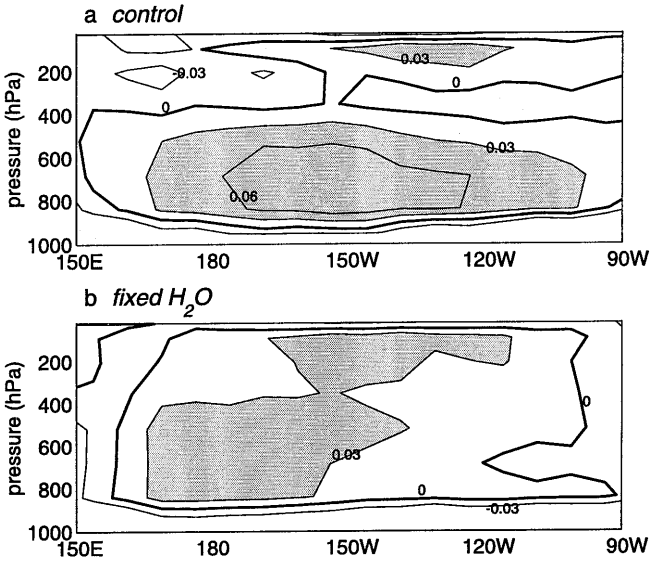

Fig. 8 **a** Longitude-height cross-section at 2.25°N of the radiative heating (°C/day) that results when the typical cloud, water vapor, and temperature changes associated with 1 °C SST anomalies in the *control* experiment are imposed on an offline version of the model's radiative transfer subroutine. Regions where the radiative heating exceeds 0.03 are shaded. The zero contour is thickened for clarity. **b** As in **a**, except for the *fixed* H_2O case

are small, we calculated the radiative heating rates that occur in both experiments when the cloud and water vapor changes associated with typical local SST anomalies are imposed simultaneously on the off-line radiative transfer code. The results are shown in Fig. 8. These changes are identical to the regressions shown in Figs. 6 and 7. The temperature changes related to typical local SST anomalies, given by the regressions between atmospheric temperature and SST, were also imposed in this calculation, since atmospheric temperature can also affect radiative heating. In the *fixed* H_2O case, water vapor was not allowed to affect the longwave portion of the off-line code, as with the actual *fixed* H_2O experiment. As expected the pattern of radiative heating seen in Fig. 4 is reasonably well-reproduced: the *control* pattern of strong heating in the lower troposphere and weaker heating or even cooling in the upper troposphere seen in Fig. 4 is also seen in this figure. Although in the *fixed* H_2O case the radiative heating is not quite as large in this figure as in Fig. 4, the general pattern is similar: the radiative heating is fairly uniform throughout the troposphere. In the lowest part of the troposphere (below 900 hPa), the patterns differ because SST was not perturbed in the offline calculation.

Since the off-line radiation code is reasonably accurate in reproducing the radiative heating patterns shown in Fig. 4, we now use it to assess the individual contributions of water vapor and clouds. As noted previously, we imposed the cloud and water vapor changes shown in Figs. 6 and 7 separately on the off-line radiation code. The results are shown in Fig. 9 for the experiment with water vapor feedback, and in Fig. 10 for the experiment

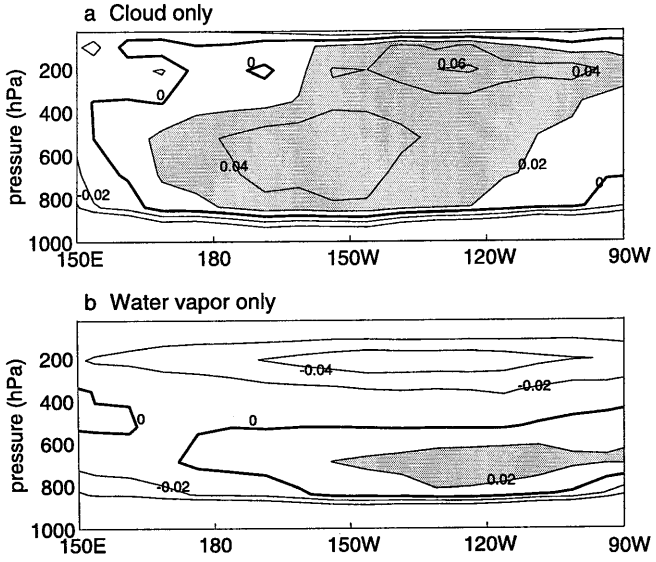

Fig. 9 **a** Longitude-height cross-section at 2.25°N of the radiative heating (°C/day) that results when the typical cloud changes associated with 1 °C SST anomalies in the *control* experiment are imposed on an offline version of the model's radiative transfer subroutine. Regions where the radiative heating exceeds 0.02 are shaded. The zero contour is thickened for clarity. **b** As in **a**, except that water vapor changes are imposed instead of cloud changes

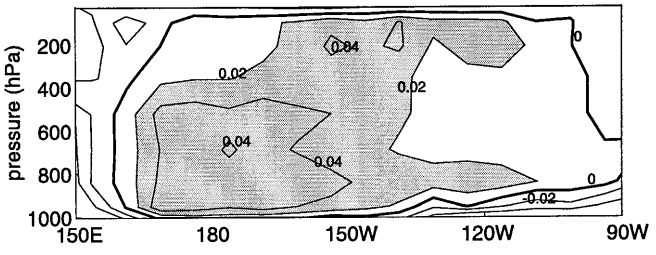

Fig. 10 Longitude-height cross-section at 2.25°N of the radiative heating (°C/day) that results when the typical cloud changes associated with 1 °C SST anomalies in the *fixed* H_2O experiment are imposed on an offline version of the model's radiative transfer subroutine. Regions where the radiative heating exceeds 0.02 are shaded. The zero contour is thickened for clarity

without. We begin by examining the radiative heating structure induced by the cloudiness changes associated with a typical *control* SST anomaly (Fig. 9a). In the western portion of the basin, there is relatively large radiative heating in the lower troposphere. In contrast, in the eastern portion, there is large radiative heating in the upper troposphere. The pattern in the central Pacific is one of uniform radiative heating throughout the troposphere. Thus in the western sector cloudiness changes reduce the gravitational stability of the atmosphere through their impact on radiative heating, while in the eastern sector they increase the atmosphere's gravitational stability. Moving to the *fixed* H_2O case, the radiative heating pattern is similar to that of the *control* case, but not identical. This is not surprising, since the cloud feedback is not the same in the two experiments, as documented in Sect. 6. However, it cannot be said that the radiative heating due to cloudiness changes associated with a typical SST anomaly cause the atmosphere in the experiment without water vapor feedback to be more stable, thereby suppressing ENSO. For example, in the *fixed* H_2O experiment cloudiness changes also induce relatively strong destabilizing radiative heating in the lower troposphere in the western portion of the basin, just as was the case in the experiment with water vapor feedback. Moreover, in the eastern part of the basin, the stabilizing heating seen in the *control* case is largely absent when water vapor feedback is removed.

Since clouds cannot explain the relatively unstable radiative heating profile in the experiment with water vapor feedback, we turn to the radiative effects of water vapor itself to explain ENSO suppression. The radiative heating due to the water vapor changes associated with a typical *control* SST anomaly (Fig. 9b) exhibits strong heating in the lower troposphere, and strong cooling in the upper troposphere. This is precisely the radiative heating structure that would systematically reduce the gravitational stability of the atmosphere. Since this structure is entirely absent in the *fixed* H_2O experiment, it is the radiative impact of water vapor, rather than clouds, that is mainly responsible for the relatively unstable radiative heating profile seen in Fig. 4a.

The typical atmospheric temperature anomalies associated with SST anomalies also affect radiative heating. However, the radiative heating profiles that result in the *control* and *fixed* H_2O cases when these temperature anomalies are imposed on the offline radiative transfer code are not shown here for two reasons. First, in both experiments, the radiative heating anomalies arising from the temperature perturbation are small compared to the anomalies arising from the cloud and water vapor perturbations. Second, the patterns of radiative heating that result from the temperature perturbation are very similar between the two experiments. Thus temperature effects are unimportant in explaining the stark difference in the vertical structure of radiative heating seen in Fig. 8.

This analysis confirms that the water vapor anomaly associated with a warm SST anomaly in the equatorial Pacific increases convection through its impact on radiative heating. Since this increased convection must be accompanied by enhanced low-level convergence, we expect a warm SST anomaly in the *control* experiment to be associated with a larger westerly anomaly in the surface easterly winds. We may verify this by examining the regressions between annual-mean zonal wind (westerly winds are positive, easterlies are negative) and SST in the equatorial Pacific. When averaged over the region corresponding roughly to the maximum in tropical Pacific SST standard deviation associated with the *fixed* H_2O model's ENSO-like phenomenon (4.5°S–4.5°N, 180°E–112.5°W), this regression reaches a value of 0.81 m/s per °C in the *fixed* H_2O experiment. In the *control* experiment, on the other hand, the regression averaged over the same region is 0.97 m/s per °C, about 20% larger. This would lead to a correspondingly larger reduction in up-

welling of relatively cold water, and greater enhancement of the original SST anomaly. Thus the interaction between longwave radiation and water vapor effectively strengthens the positive feedback between SST and wind-stress. The absence of water vapor feedback, on the other hand, weakens this coupling, resulting in a decrease in the magnitude of simulated ENSO events.

The weakening of the unstable air-sea interactions of the equatorial Pacific in the *fixed* H_2O experiment reduces not only the magnitude of the model's ENSO-like phenomenon, but also its geographical extent. We noted in Sect. 5 that a typical warm event in the *control* experiment extends further east than its *fixed* H_2O counterpart. Consistent with this result, we also showed in Sect. 7 that the relative effectiveness of *control* SST anomalies in inducing anomalies of the same sign of convection, cloudiness, and water vapor is particularly apparent in the central and eastern portions of the basin. This is because SST anomalies are not equally effective in inducing convection at all longitudes (Keshavamurti 1982). To expand the convective region from the western equatorial Pacific to any given location in the central to eastern equatorial Pacific, SST in the newly convecting regions must be high enough to be comparable to SST in the western portion of the basin. Since equatorial Pacific SST increases going from east to west in both the model and the real world, the SST anomalies required to satisfy this condition increase going toward the east. Thus while the magnitudes of the ENSO-related SST anomalies are smaller in the experiment without water vapor feedback at all equatorial Pacific locations, the impact of the difference in magnitudes is much larger in the central to eastern portion of the basin. Here, the ENSO-related SST anomalies in the *fixed* H_2O experiment are too small to bring SST to the critical threshold required to expand the convective region to this location. This reduces further the coupling between SST and wind-stress beyond the reduction due to the absence of water vapor feedback, thereby reducing ENSO variability in this region even more.

8 Summary and discussion

We have shown that, although an ENSO-like phenomenon is present in both experiments, its amplitude is significantly smaller and its geographical extent more limited in the experiment without water vapor feedback. Surprisingly, increased longwave radiative damping of equatorial Pacific SST anomalies in the *fixed* H_2O case cannot explain the ENSO suppression: differences between the two experiments in radiative feedbacks due to clouds counterbalance almost perfectly the differences due to water vapor. However, the cause of the ENSO suppression can be traced to the interaction of longwave radiation and water vapor. Because of the changes in water vapor associated with it, a given warm equatorial Pacific sea surface temperature anomaly is related to a radiative heating profile that is much more gravitationally unstable when water vapor feedback is present. As a result, more convection is associated with a typical warm equatorial Pacific SST anomaly in the *control* experiment. The increased convection, in turn, is accompanied by a larger westerly wind-stress anomaly, which creates a larger decrease in upwelling of cold water, thereby enhancing the magnitude of the original warm SST anomaly. In this manner, the interaction between water vapor anomalies and longwave radiation magnifies the classic instability of equatorial Pacific air-sea interactions at the heart of the ENSO phenomenon; without this interaction, the coupling between SST and wind stress is effectively reduced, resulting in smaller amplitude ENSO episodes with a more limited geographical extent. These results reveal the importance of water vapor feedback, and radiative processes in general, for the simulation and prediction of ENSO using fully coupled ocean-atmosphere models.

These results also add a new element to the classical picture of tropical convection. It is commonly held that the response of the tropical atmosphere to a warm SST anomaly can be understood in terms of conditional instability of the second kind (CISK), an idea first set forth by Charney and Eliassen (1964). In this scenario, a warm SST anomaly induces evaporation, thereby reducing the moist static stability of the atmosphere. If the lower atmosphere becomes unstable enough, convection and low-level convergence occur. The low-level convergence drives evaporation and moisture transport into the convective region, which maintain the low moist static stability of the lower atmosphere, thereby amplifying the convection associated with the warm SST anomaly. According to our results, another positive feedback process plays an important role in the response of the tropical atmosphere to a warm SST anomaly. In this scenario, radiative heating stemming from water vapor feedback helps to determine the amount of convection a warm SST anomaly induces: once the evaporation resulting from a warm SST anomaly reduces the moist static stability of the atmosphere enough to induce convection, the resulting penetration of water vapor into the upper troposphere produces a radiative heating profile characterized by heating in the lower troposphere and cooling in the upper troposphere. This helps to maintain the low moist static stability of the lower troposphere, thereby facilitating continued convection, additional penetration of water vapor into the upper troposphere, and more destabilizing radiative heating. In the present model, this mechanism also has a significant effect on the atmospheric response to a warm SST anomaly.

Finally, it was noted in Sect. 4 that the relatively coarse computational resolution of this model is the main reason why its ENSO is weaker than observed. Therefore, it is desirable to repeat this type of study using a higher resolution model to see if the conclusions are still robust when the simulated ENSO events are similar in magnitude to the observed.

Acknowledgements The authors wish to thank Tom Knutson and Isaac Held for helpful discussions and constructive criticism of the manuscript. In addition, the authors are grateful to two anonymous reviewers. Alex Hall was supported by a NASA Earth System Science Fellowship while this research was being carried out. Finally, the authors wish to thank the Geophysical Fluid Dynamics Laboratory for making available the computational resources required to carry out these experiments.

References

Bjerknes J (1969) Atmospheric teleconnections from the equatorial Pacific. Mon Weather Rev 97: 163–172

Bryan K (1969) Climate and the ocean circulation: III. The ocean model. Mon Weather Rev 97: 806–827

Bryan K, Lewis L (1979) A water mass model of the world ocean. J Geophys Res 84(C5): 2503–2517

Chao Y, Philander SGH (1993) On the structure of the Southern Oscillation. J Clim 6: 450–469

Charney J, Eliassen A (1964) On the growth of the hurricane depression. J Atmos Sci 21: 68–75

Hall A, Manabe S (1999) The role of water vapor feedback in unperturbed climate variability and global warming. J Clim 12: 2327–2346

Julian PR, Chervin RM (1978) A study of the Southern Oscillation and Walker Circulation phenomenon. Mon Weather Rev 106: 1433–1451

Keshavamurty RN (1982) Response of the atmosphere to sea surface temperature anomalies over the equatorial Pacific and the teleconnections of the Southern Oscillation. J Atmos Sci 39: 1241–1259

Knutson TR, Manabe S (1994) Impact of increased CO_2 on simulated ENSO-like phenomena. Geophys Res Lett 21: 2295–2298

Knutson TR, Manabe S, Gu D (1997) Simulated ENSO in a global coupled ocean-atmosphere model: multidecadal amplitude modulation and CO_2 sensitivity. J Clim 10: 138–161

Lau NC, Philander SGH, Nath MJ (1992) Simulation of ENSO-like phenomena with a low-resolution coupled GCM of the global ocean and atmosphere. J Clim 5: 284–307

Manabe S, Wetherald R (1967) Thermal equilibrium of the atmosphere with a given distribution of relative humidity. J Atmos Sci 24: 241–259

Manabe S, Stouffer RJ, Spelman M, Bryan K (1991) Transient responses of a coupled ocean-atmosphere model to gradual changes of atmospheric CO_2. Part I: annual mean response. J Clim 4: 785–817

Marotzke J, Stone P (1995) Atmospheric transports, the thermohaline circulation, and flux adjustments in a simple coupled model. J Phys Oceanogr 25: 1350–1364

Neelin JD (1991) The slow sea surface temperature mode and the fast-wave limit: analytic theory for tropical interannual oscillations and experiments in a hybrid coupled model. J Atmos Sci 48: 584–606

Neelin JD, Latif M, Jin F (1994) Dynamics of coupled ocean-atmosphere models: the tropical problem. Annu Rev Fluid Mech 26: 617–659

Pacanowski R, Dixon K, Rosati A (1991) The GFDL Modular Ocean Model Users Guide. GFDL Ocean Group Technical Rep 2

Rassmusson EM, Carpenter TH (1982) Variations in tropical sea surface temperature and surface winds associated with the Southern Oscillation. Mon Weather Rev 110: 354–384

Redi MH (1982) Oceanic isopycnal mixing by coordinate rotation. J Phys Oceanogr 12: 1154–1158

Schopf PS, Suarez MJ (1988) Vacillations in a coupled ocean-atmosphere model. J Atmos Sci 45: 549–566

Trenberth KE, Shea DJ (1987) On the evolution of the Southern Oscillation. Mon Weather Rev 115: 3078–3096

Tziperman E, Bryan K (1993) Estimating global air-sea fluxes from surface properties and from climatological flux data using an oceanic general circulation model. J Geophys Res 98(C12): 22629–22644